

# Ex Vivo Validation of Magnetically Actuated Intravascular Untethered Robots in a Clinical Setting

**Islam Khalil** (✉ [i.s.m.khalil@utwente.nl](mailto:i.s.m.khalil@utwente.nl))

Biomechanical Engineering

**Leendert-Jan Ligtenberg**

Biomechanical Engineering

**Nicole Rabou**

Biomechanical Engineering

**Constantinos Goulas**

Biomechanical Engineering

**Wytze C. Duinmeijer**

Biomechanical Engineering

**Frank R. Halfwerk**

Biomechanical Engineering

**Jutta Arens**

Massachusetts General Hospital

**Roger Lomme**

Radboud University Medical Center

**Veronika Magdanz**

University of Waterloo

**Anke Klingner**

German University in Cairo

**Emily Klein Rot**

LipoCoat B.V

**Colin H.E. Nijland**

LipoCoat B.V

**Dorothee Wasserberg**

LipoCoat B.V

**Pascal Jonkheijm**

LipoCoat B.V

**H. Liefers**

University of Twente

**Arturo Susarrey-Arce**

University of Twente

**Michiel Warle**

## Article

### Keywords:

**Posted Date:** December 4th, 2023

**DOI:** <https://doi.org/10.21203/rs.3.rs-3526473/v1>

**License:**  This work is licensed under a Creative Commons Attribution 4.0 International License.

[Read Full License](#)

**Additional Declarations:** There is **NO** Competing Interest.

---

# *Ex Vivo* Validation of Magnetically Actuated Intravascular Untethered Robots in a Clinical Setting

Leendert-Jan W. Ligtenberg,<sup>1</sup> Nicole Rabou,<sup>1</sup> Constantinos Goulas,<sup>2,3</sup>  
Wytze C. Duinmeijer,<sup>1,3</sup> Frank R. Halfwerk,<sup>1,3</sup> Jutta Arens,<sup>1,3</sup>  
Roger Lomme,<sup>4</sup> Veronika Magdanz,<sup>5</sup> Anke Klingner,<sup>6</sup>  
Emily A.M. Klein Rot,<sup>7</sup> Colin H.E. Nijland,<sup>7</sup> Dorothee Wasserberg,<sup>7,8</sup>  
H. Remco Liefers,<sup>3</sup> Pascal Jonkheijm,<sup>7,8</sup> Arturo Susarrey-Arce,<sup>9</sup>  
Michiel Warlé,<sup>6\*</sup> Islam S. M. Khalil<sup>1,3\*</sup>

<sup>1</sup>Department of Biomechanical Engineering, University of Twente,  
7500 AE Enschede, The Netherlands

<sup>2</sup>Department of Design Production and Management, University of Twente,  
7500 AE Enschede, The Netherlands

<sup>3</sup>Technical Medical Centre, University of Twente,  
7500 AE Enschede, The Netherlands

<sup>4</sup>Radboud University Medical Center,  
6525 GA Nijmegen, The Netherlands

<sup>5</sup>Department of System Design Engineering, University of Waterloo,  
ON N2L 3G1 Waterloo, Canada

<sup>6</sup>Department of Physics, German University in Cairo,  
New Cairo 11835, Egypt

<sup>7</sup>LipoCoat B.V., 7521 AG Enschede, The Netherlands

<sup>8</sup>Laboratory of Biointerface Chemistry, TechMed Centre, University of Twente,  
7500 AE Enschede, The Netherlands

<sup>9</sup>Mesoscale Chemical Systems, MESA+ Institute, University of Twente,  
7500 AE Enschede, The Netherlands

**Intravascular surgical instruments necessitate precise navigation within nar-**

row vessels, requiring maximum flexibility, minimal diameter, and high degrees of freedom. However, existing tools often lack adequate control during insertion due to undesirable bending, which not only limits vessel accessibility but also poses a risk of tissue damage. The advancement of next-generation instruments aims to develop hemocompatible untethered devices that achieve precise control through external wireless forces and torques applied from outside the body. However, achieving this goal remains complex due to the challenges involved in testing and implementing untethered magnetic robots (UMRs) in clinical environments. These challenges encompass wireless actuation, non-invasive localization, biocompatibility, control robustness, and effective engagement. In this study, we assess the operational effectiveness of hemocompatible UMRs in clinical settings. We utilize an *ex vivo* porcine aorta model that accounts for factors such as varying blood-vessel diameters, varying blood flow rates, and the presence of renal aortic side-branches. This comprehensive approach enables us to analyze the robots' motion dynamics within vessels, closely simulating real physiological and anatomical conditions. Our findings, in the absence of clotting, reveal a consistent linear reduction in UMR swimming speed against increasing arterial blood flow. Furthermore, our experiments showcase the UMR's ability to generate sufficient force to navigate against a maximum arterial flow rate of 67 mL/min. Using the predicted and observed physical interactions of the UMRs, we effectively demonstrate preliminary proof-of-concept locomotion in a difficult-to-access target site, allowing us to navigate through the abdominal aorta and successfully reach the distal end of the renal artery.

## INTRODUCTION

Untethered magnetic robots (UMRs) have the potential to navigate through bodily fluids for surgical or therapeutic procedures, such as targeted therapy and material removal. When operating *in vitro*, the navigation of UMRs is often greatly simplified by a controlled environment in which detailed analysis of one or more important physical effects are studied inside petri dishes or test tubes. This type of experiments has allowed to advance our knowledge about the incorporation of a specific physical intelligence into UMRs, which is significantly important at small scales, allowing them to be used as end-effectors of wireless manipulation systems (1, 2). Microactuation (3), high-precision transportation and cargo delivery (4, 5), gamete transport (6, 7), microassembly (8, 9), diagnosis (10), material removal and targeted drug delivery (11) have been demonstrated *in vitro* at a number of scales (12). While these promising experiments have indeed demonstrated the significant potential of UMRs across various technologies and therapies, it is important to acknowledge that they currently fall short of replicating the intricate conditions found within living organisms. As a result, the full extent of their capabilities and limitations remains unexplored.

It is unlikely that UMRs can effectively be used *in vivo* unless multiple hurdles are addressed simultaneously, such as wireless power (13), locomotion (14, 15), localization (16, 17), control robustness (18), and biocompatibility (19). Consider, for example, a scenario where reaching a particular location proves challenging through conventional tethered methods (Figure 1A) (20). In this case, the UMR would be inserted in either fluid-filled lumen or soft tissue, allowing access to the whole human body by swimming through bodily fluids or drilling through tissue, or both. This is most practically done through a UMR designed with a chiral geometry (e.g., screw-shaped or helical body), which can be driven by homogeneous rotating magnetic fields (21–24). To achieve the objective of reaching its location, the UMR must effectively

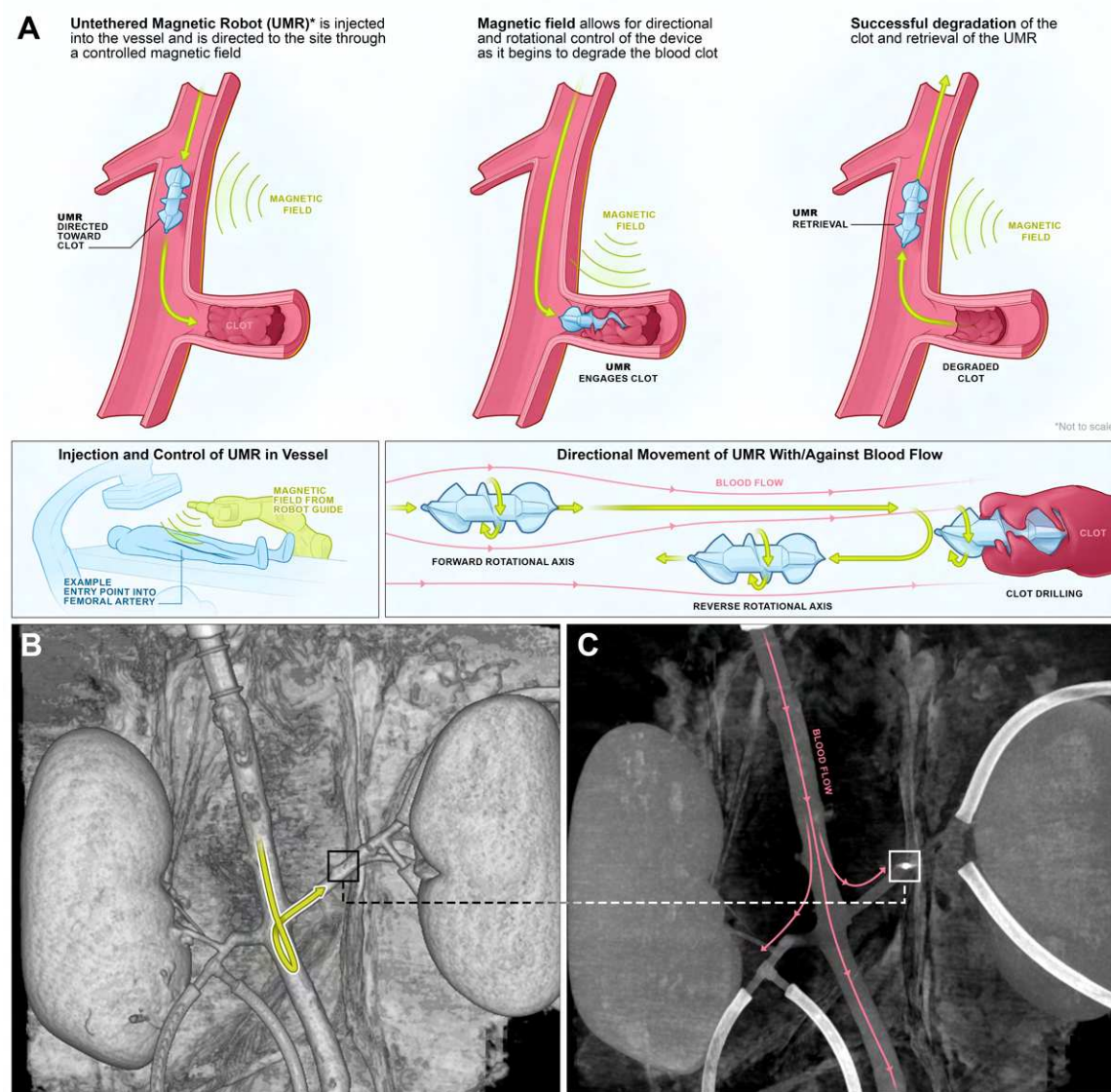


**Fig. 1. The untethered magnetic robot (UMR) can swim inside natural pathways of a porcine aorta model under controlled conditions, enabling interventions and retrieval with minimal incisions.** (A) The wireless actuation and non-invasive localization of UMRs are achieved through a robotic platform. UMRs navigate both with and against the blood flow for various interventions. (B)-(C) A 9-mm-long UMR moves both with and against the blood flow inside the abdominal aorta and is then guided to swim within the left renal artery. The UMR's location is highlighted by squares in the CBCT-scans, and its trajectory is depicted by the yellow arrow (movie S1).

harness sufficient mechanical energy for its locomotion while contending with the dynamics of blood circulation. To reach the desired location in Fig. 1A, the UMR must be steered controllably at bifurcations and driven with optimal rate at which maximum propulsive thrust is achieved. This scheme requires that we localize the UMR, reconstruct its physical surroundings, and achieve an acceptable level of biocompatibility and control robustness using a robotic platform at a scale relevant for clinical use. Even then, the true capabilities of these devices can only be conclusively demonstrated through *ex vivo* and *in vivo* experimental results. This is due to the complex interplay of multiple physical effects (such as the wall effect, blood flow, vessel bifurcations, and magnetohydrodynamic coupling), which cannot be accurately replicated *in vitro*.

In order for UMRs to realize their anticipated potential in the field of biomedicine, it is imperative to bridge the existing credibility gap by effectively tackling the challenges mentioned earlier. In recent years, there has been some progress in realizing wireless control of UMRs *in vivo*. Niedert *et al.* have successfully maneuvered a tumbling microrobot within a live mouse's colon, employing an external time-periodic magnetic field and an ultrasound imaging system. However, a notable challenge lies in the restricted field-of-view during localization, consequently confining the procedure's applicability to smaller animals exclusively (25). In contrast, Vonthrom *et al.* have utilized a clinical magnetic resonance imaging (MRI) system (large enough to provide a strong field gradient over the human body) to localize, steer, and control microrobots and microdevices (26). In this case, MRI systems generate wide field-of-view images for localization and control with adequate resolution. However, the locomotion of torque-driven UMRs is limited by the MRI systems, which allows for partial control as field gradients can only be scaled. Similarly, Tiryaki *et al.* have shown an MRI-powered magnetic miniature capsule robot capitalizing on acoustic streaming forces generated by high-intensity focus ultrasound for controlled drug release (27). However, for ferromagnetic torque-driven

UMRs actuated by homogeneous magnetic fields, MRI systems become unfeasible as high magnetic field associated with imaging would interfere with the magnetization and magnetic response. Therefore, there is a need to mitigate the influence of the field associated with the imaging instrumentation on that of the wireless actuation. Servant *et al.* have used feedback of an optical fluorescence imaging system to control a swarm of functionalized artificial bacterial flagella (ABFs) *in vivo* (28). In this scenario, the ABFs are functionalized with near-infrared fluorophores for the purpose of tracking within the intraperitoneal cavity of a small anesthetized animal. The animal is enclosed by coils to facilitate wireless actuation. While this optical technique facilitates comprehensive whole-body imaging, the challenge remains in effectively tracking UMRs within deep tissues and vessels, posing a notable hurdle.

Here we translate UMRs into *ex vivo* trials and achieve directional control inside a porcine aorta model with varying blood vessel diameter. Figs. 1B and 1C (Movie S1) show the path taken by a UMR, against and with arterial flow, toward the distal end of the renal artery, visualized by two cone-beam computed tomography (CBCT)-scans. To achieve this level of control, we assess the UMR's swimming behavior in a porcine aorta model in a clinical setting (Figures 2A and 2B) by using wireless actuation and localization systems that can be effectively scaled up (Figs. 2C-2F). Initially, we undertake the design and characterization of UMRs that possess the ability to navigate through the whole porcine aorta model. The magnetic behavior of these UMRs in response to an external actuating magnetic field is assessed through an *in vitro* blood vessel model. Notably, only extended-duration characterization experiments are conducted *in vitro*. The predictions for optimal actuation inputs—specifically, actuation frequency and magnetic field strength—are made using ultrasound images and are correlated with the fluid properties. Subsequently, with these calculated inputs, we successfully showcase that UMRs are capable of controlled movement within confined spaces. This controlled movement enables the UMRs to navigate the interior of blood vessels in the porcine aorta model while



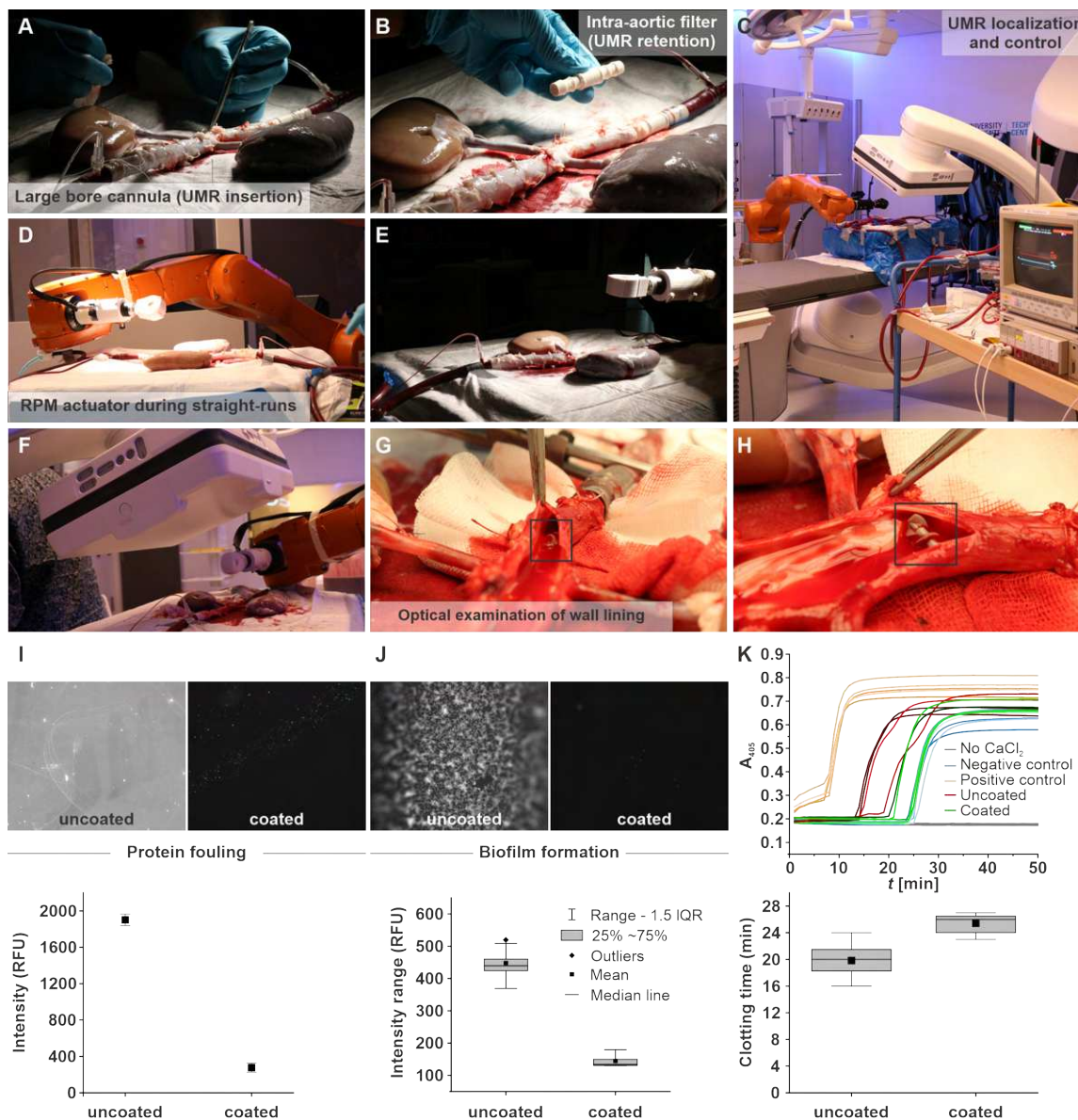


**Fig. 2. *Ex vivo* trials are conducted using a porcine aorta model.** (A) The *ex vivo* organs are harvested and connected to a circulation pump prior to each motion control session. (B) Placement of an intra-aortic 3D printed filter allows the UMR to remain inside the aorta irrespective of the ongoing blood circulation. (C)-(F) Wireless magnetic actuation and C-ARM imaging systems enable control and localization, respectively. (G)-(H) Optical examination of the internal wall lining of the vessels shows no risk of damage by the UMR. The black squares indicate the UMR. (I)-(K) Hemocompatibility tests included (I) protein fouling, (J) biofilm formation and (K) coagulation evaluation.

minimizing contact with the vessel walls (Figs. 2G and 2H). In order to assure hemocompatibility of the UMRs a lipid-based coating was applied and various assay were carried out to verify this hemocompatibility. Fig. 2I shows micrographs of coated UMR material after incubation with fluorescently-labeled fibrinogen. Fibrinogen adsorption on the coated samples is reduced by 95% compared to the uncoated samples. Fig. 2J shows micrograph images of biofilms formed by *Staphylococcus aureus* on coated and uncoated samples, with a reduction of more than 99%. Fig. 2K compares the fibrin generation in time, of platelet-poor plasma in contact with coated versus uncoated samples. Fibrin generation was delayed by  $> 6$  min for the coated samples compared to the uncoated samples. Together with further assays (see Methods) the data indicates that no detrimental effect of coated UMRs is expected during *in vivo* applications.

## RESULTS

### *Ex vivo* model and robotic platform

Leveraging the detailed understanding of the aorta’s anatomy and physiology (see Methods), we are able to evaluate the swimming capabilities of the UMRs. By conducting straight runs within the abdominal aorta, we can observe the UMRs’ swimming behavior both against and with the blood flow. Additionally, the setting of the renal aortic side-branch offers a suitable environment for assessing the UMRs’ ability to achieve directional control (Figs. 1B and 1C). The proximal and distal ends of the abdominal aorta are connected to a peristaltic pump for blood circulation at controlled flow rate in the  $15 \leq \dot{Q} \leq 260$  mL/min range. The UMR comprises a screw-shaped body, created through additive manufacturing, with affixed permanent magnet. Through the addition of a lipid-based coating, the UMR can attain self-sufficiency and maintain cellular viability (29). The lipid-based coating has been shown to be highly hemocompatible, activating neither of the clotting pathways nor the complement system (see Methods and Fig. S1 for more

detailed information). Because of the miniature permanent magnet, we avoid the need to create strong magnetizing fields. The UMR is inserted into the model from the proximal end of the abdominal aorta through a large bore cannula (Fig. 2A). An intra-aortic 3D printed filter is connected to the distal end of the aorta (Fig. 2B) to retain the UMR when the applied blood flow is much greater than its propulsive thrust, or when the UMR is not magnetically coupled with the rotating permanent magnet (RPM) actuator, temporarily. The *ex vivo* model and the RPM-actuator are placed between an X-ray source and a detector, as shown in Figs. 2C-2F. As the X-ray beam traverses through the model, the affixed UMR magnet, and the RPM-actuator, its intensity is diminished. This attenuation occurs as the X-ray travels from the source to the detector array. Consequently, the acquired CBCT-scan data enables us to reconstruct the internal structure of the model in 3 dimensions with precision, as shown in Figs. 1B and 1C, which would be useful in examining the positioning accuracy after actuation.

In contrast, X-ray Fluoroscopy images are gathered online with good resolution and at adequate frame rate (5 frames per second) for direct teleoperation, allowing the UMR to swim controllably under the influence of external inputs given directly by a clinician. Figure 3A shows an X-ray Fluoroscopy image during a straight-run inside the abdominal aorta. A rotating magnetic field is generated by the RPM-actuator, which is directly teleoperated based on the gathered X-ray Fluoroscopy images. Our robotic platform (i.e., C-Arm and wireless manipulation system) is configured such that the UMR, its physical surroundings, and the RPM-actuator are captured in each X-ray Fluoroscopy image, as shown in Fig. 3A. This is accomplished by using an oblique angle for the X-ray source and the detector array (Fig. 3B). The source and the detector of the C-Arm imaging system are kept at an oblique angle of  $20^\circ$  with the  $z$ -axis (in the frame of reference in Fig. 3). This setup enables the captured X-ray Fluoroscopy images to clearly display both the UMR and the RPM-actuator, thereby enhancing the intuitiveness of teleoperation. Furthermore, the oblique orientation of the C-Arm offers the RPM-actuator an

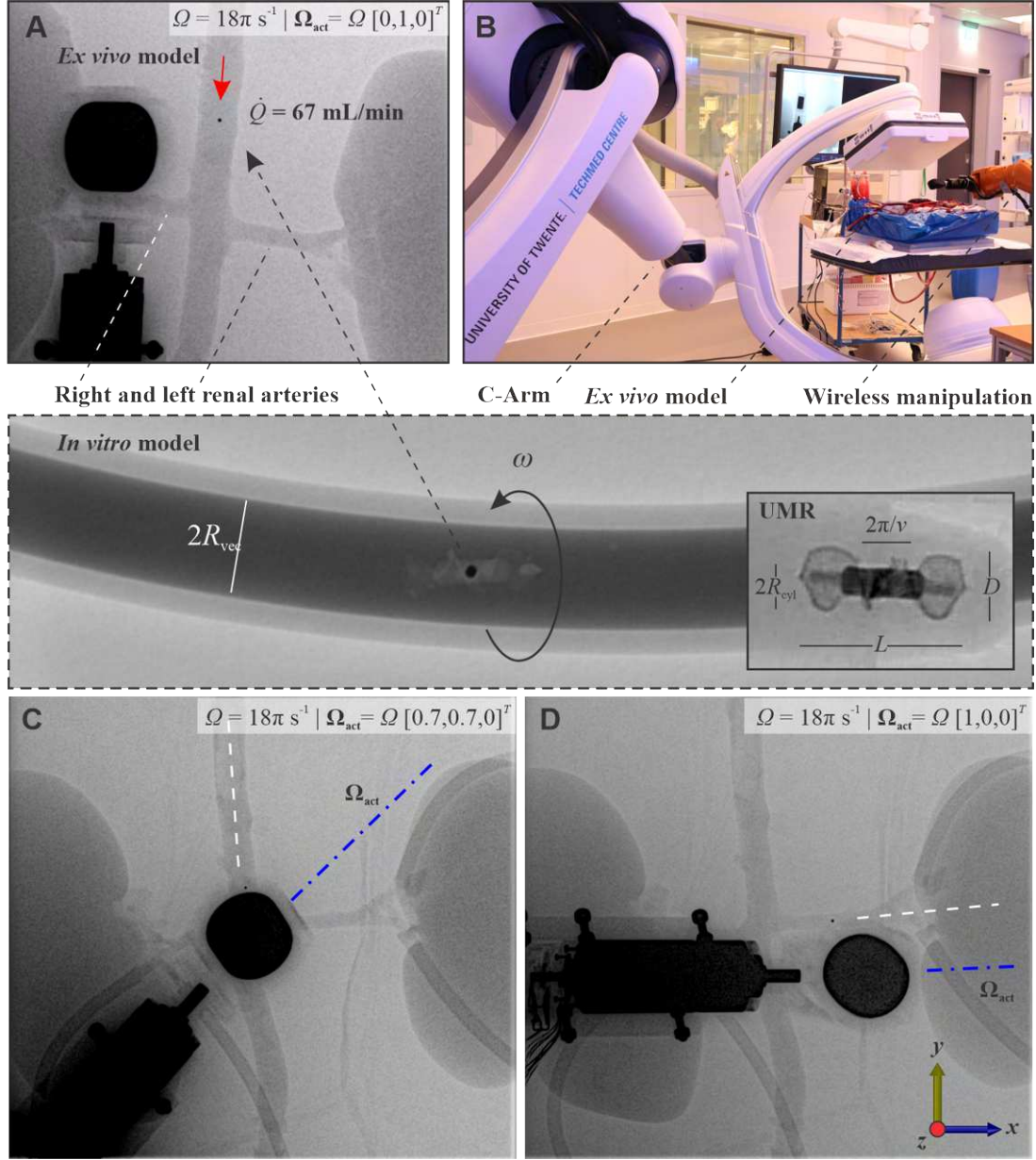


**Fig. 3. UMRs are employed to navigate vascular pathways for interventions.** (A) X-Ray Fluoroscopy images are gathered online to detect the UMR, the RPM-actuator, and the physical surroundings using clinically relevant radiation settings. To show the shape of the UMR, a radiocontrast agent is injected into an *in vitro* model. (B) Our robotic platform consists of a C-Arm imaging and permanent magnet robotic systems. (C)-(D) The process of steering and maneuvering the UMR within the left renal artery is achieved by manipulating the rotation axis of the RPM about the  $z$ -axis.

expanded workspace, minimizing the potential for interference with the detector array.

Fig. 3A shows the configuration of the RPM-actuator and the position of the UMR during a straight-run against arterial flow. In this case, the RPM rotation axis,  $\Omega_{\text{act}}$ , is oriented parallel to the centerline of the abdominal aorta and its translational velocity is controlled such that it remains in sync with the UMR. The insets illustrate the UMR's geometry, achieved by introducing a radiocontrast agent into an *in vitro* model (refer to Methods), enhancing visibility of the radiolucent structure. Nevertheless, under clinically relevant radiation doses, the low contrast resolution solely yields a detectable signal from the attached radiopaque magnet. Consequently, solely the magnet of the UMR becomes visible in the X-ray Fluoroscopy images in Figs. 3A, 3C, and 3D. Although controlling the UMR is challenging without orientation information at this radiation level (Fluoroscopy dose rate of:  $0.35 \text{ mGy}\cdot\text{cm}^2\text{s}^{-1}$ ), the magnetic torque would ultimately allow the UMR to align with the RPM rotation axis. This is the method used in Fig. 3C to steer the UMR and enter the left renal artery, as shown in Fig. 3D.

## Hemobiocompatibility of UMRs

Previously, we have shown that cell adhesion, cell morphology, focal adhesion formation, cell proliferation, and cell differentiation potential remain unaffected by the coating components (30). Here, we investigate biocompatibility *in vitro* in terms of protein fouling, biofilm formation, and various hemocompatibility assays. These tests are conducted using coated UMR- and other materials. It is well-established that the initial step of the surface-activated (intrinsic) pathway of the clotting cascade involves the interaction of a protein (factor XII) with a foreign substrate. Similarly, the complement system is activated through protein interactions (31). Hence, the affinity of proteins for a material is believed to be a significant determinant of a material's hemocompatibility (32). To evaluate this critical protein-material affinity, fibrinogen (clotting Factor I) is selected for use in a protein fouling assay. Microscopy of coated UMR

material after incubation with fluorescently-labeled fibrinogen revealed a 95% reduction in protein adsorption compared to uncoated UMR material (Fig. 2I). This reduction in protein fouling is expected to diminish the activation of the clotting cascade and complement system during *in vivo* use.

Bacterial infections pose a significant and prevalent risk when using medical devices (33). Bacteria that adhere to medical devices often lead to severe complications and can contribute to the formation of biofilms, which are challenging to treat and can promote antibiotic resistance (34). Therefore, we conducted an assessment to inhibit bacterial attachment and subsequent biofilm formation on coated samples, initially focusing on attachment. In this regard, both coated and uncoated PU catheter materials were exposed to *Staphylococcus aureus* for 3 days, followed by washing, staining with propidium iodide, and imaging using a fluorescence microscope. The results indicated that the coated samples exhibited a reduction of over 99% in attached bacteria compared to the uncoated samples. This underscores the potential of using coated UMRs to reduce the risk of infection when compared to their uncoated counterparts. In the case of short dwell time UMRs, the primary infection risk appears to stem from bacterial introduction during insertion, rather than supporting biofilm formation.

Another common hemocompatibility assay is the fibrin generation test (35, 36). It is routinely used to assess the formation of fibrin fibres, which, together with platelets, constitute the final stage of the clotting cascade, the blood clot. For the independent assessment of the intrinsic pathway, fibrin formation was tested using platelet poor plasma (PPP) isolated from freshly drawn, citrated whole-blood. Coated and uncoated UMR material was immersed in citrated PPP and, subsequently, the clotting cascade was re-initiated by reconstituting  $\text{Ca}^{2+}$  to physiological levels. The clotting cascade eventually leads to the formation of fibrin fibres, which causes a sudden increase in light scattering. The scatter signal at 405 nm is monitored in time, starting immediately after initiation. A sharp increase in the scatter signal, denotes the start of

fibrin generation and can be accelerated by materials incompatible with the *in vivo* environment. Comparing coated with uncoated UMR material, a maximum of 6 min delay in fibrin formation was observed for the coated material. Thus, the coated material clearly delays the clotting via the intrinsic pathway and, therefore, coated UMRs are expected to carry a reduced embolic risk *in vivo* compared to uncoated UMRs.

LipoCoat 4AC coated PU catheter material was subjected to a variety of hemocompatibility tests carried out by a company dedicated to hemocompatibility testing of blood contacting devices, HAEMOSCAN BV. Standard hematology tests were carried out, consisting of platelet and red blood cell counts as well as quantification of hemoglobin and material-induced hemolysis. Thrombus tests included, visual and gravimetric assessment of thrombi formed on the samples, quantification via immunostaining of fibrin adsorbed to the samples and enzymatic quantification of attached platelets. Platelet activation was tested by quantifying released thromboxane B2 and beta thromboglobulin as well as platelet aggregation. Coagulation tests consisted of the quantification of thrombin-antithrombin III complex and fibrinopeptide A. Inflammation and complement activation were assessed by quantifying complement component fragments C3a-desArg and C5b-9 as well as elastase. The coated samples passed all hemocompatibility tests at levels comparable if not better than the negative control. The entirety of the data discussed above indicates coated samples to be highly hemocompatible and to expect no issues with regard to coagulation nor complement activation during *in vivo* use.

## **Wireless locomotion of UMRs in arterial flow**

The movement of screw-shaped UMRs within low- $Re$  (on the order of  $10^{-1}$ ) blood flow depends on three significant physical phenomena. The initial effect involves drag anisotropy, crucial for generating a net propulsive thrust through lateral movement or rotation around the long axis of the UMR. This characteristic is attained through the screw-shaped configuration



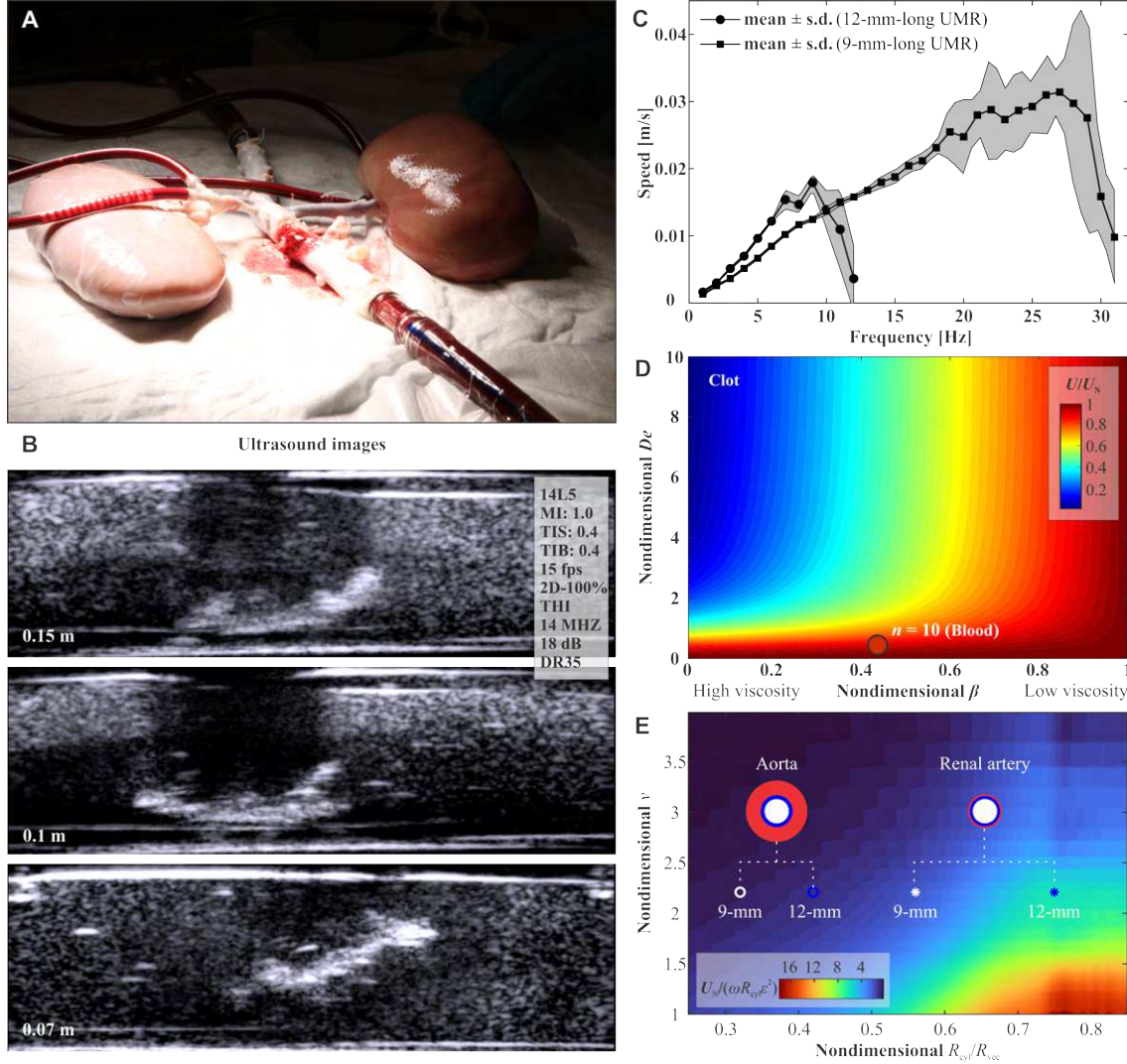


**Fig. 4.** The movement of the UMR is influenced by several factors, including the constraints imposed by the *ex vivo* model's confinement, the viscosity of the blood, and the external control inputs applied. (A)-(B) The actuation of the UMR is evaluated by utilizing ultrasound images to identify an optimal gap between the RPM and the UMR. This gap is determined to achieve enough RPM clearance while minimizing contact with the inner wall of the lumen. (C) Frequency response of the UMR is characterized in blood. (D) Prediction of swimming speed of a UMR in blood and through a clot. The speed of the UMR,  $U$ , is normalized with swimming speed,  $U_N$ , in a Newtonian fluid (water). (E) The UMR's swimming speed is influenced by the normalized wavenumber  $\nu = \nu^* R_{cyl}$  and diameter of the surrounding vessel ( $2R_{ves}$ ). The white and blue markers indicate the small and large UMRs used in our study, which share the same normalized helical pitch ( $2\pi/\nu$ ) but differ in their ratios of  $R_{cyl}/R_{vec}$ .



of the body (refer to Methods). In this case, the helical pitch,  $2\pi/\nu$ , is a crucial design feature which can be optimized to yield sufficient thrust. The second effect is the impact of the lumen wall. This wall effect becomes significant within restricted spaces and is anticipated to increase the swimming speed for a given helical pitch of the UMR. However, within confinement, the swimming speed demonstrates an increase up to a local maximum and subsequently declines to a local minimum as the helical pitch decreases (38). As a result, when encountering blood vessel diameters of different sizes, the interplay between drag anisotropy and confinement effects would lead to fluctuations in the UMR's swimming speed as it advances. The third physical phenomenon is the magnetic interaction between the RPM-actuator and the UMR. When UMRs are intended to navigate toward a specific vessel, such as choosing one of three pathways at a bifurcation in the model, the process requires the generation of at least two magnetic torque components simultaneously. A time-periodic torque component about the long axis of the UMR would be responsible for the time-averaged propulsion, while another in-plane torque (in the  $xy$ -plane about the  $z$ -axis) would be responsible for steering. Note that the *ex vivo* model is naturally constrained to lie on the horizontal plane (Figure 4A), and therefore only these torques are sufficient to navigate and target any location of interest. Taking these effects into consideration results in a managed reaction of the UMR within the vessels. However, accessing the renal artery could remain challenging if the alignment between the UMR's long axis and the local tangent at the entry point of the centerline is not precise. In such cases, only UMRs with dimensions slightly smaller than those of the abdominal aorta and renal artery might have the potential to reach specific points of interest.

Fig. 4B displays ultrasound images of a UMR designed to fit through the renal artery upon being deployed in the abdominal aorta. The distance between its long axis and the tube's centerline varies with the UMR-RPM gap. Adjustment of the UMR-RPM gap is achievable by moving the RPM closer to the vessel, which in turn influences the UMR's proximity to the

vessel's centerline. This distance is limited to approximately 0.1 m due to the RPM's field. Alternatively, the UMR-RPM gap can be reduced further to increase the applied field, a control input that proves particularly valuable when dealing with a UMR at the onset of step-out (i.e., the frequency beyond which the UMR cannot keep pace with the actuating field). By moving the RPM-actuator closer to the vessel, the step-out frequency in such cases can be elevated. The step-out frequency of two UMRs (9-mm- and 12-mm-long) is shown in Fig. 4C, for an RPM-UMR gap of 0.1 m. Associated with the increase in the actuation frequency of the RPM is a linear increase in the swimming speed of the UMR in blood,  $U$ , and similar response is observed in water  $U_N$ . Slightly below step-out (i.e., 10 Hz), the swimming speed of the 12-mm-long UMR is greater than that of any other actuation frequency, making it favorable for actuation. In contrast, the 9-mm-long UMR boasts a wider frequency range and can be actuated at frequencies of up to 27 Hz.

In contrast to swimming in water, the interaction between blood and UMR is not solely elastic, as depicted in Fig. 4D. In the case of blood with a specific ratio of serum viscosity to total viscosity denoted as  $\beta$ , the UMR's swimming speed diminishes with higher fluid relaxation, indicated by  $De$ . The application of the Oldroyd-B model (outlined in the Methods section) offers predictions for the UMR's swimming speed across a spectrum of blood solvent viscosity ratios and relaxation values. If the viscosity of the blood were to increase to the point where  $\beta$  approaches zero, the resultant swimming speed would also tend toward zero. In a potential medical intervention scenario (as shown in Fig. 1A), a UMR might need to be moved toward a blood clot to reinstate local flow. In this instance, it is more instructive to predict its response using our model. Our UMR speeds, scaled by their speed in a Newtonian fluid ( $U/U_N$ ), are noticeably slower in clots compared to their speeds in blood. Therefore, for our experiments, it suffices to demonstrate controlled locomotion toward a specific location of interest, and potentially facilitate the release of a drug to reinstate the flow.

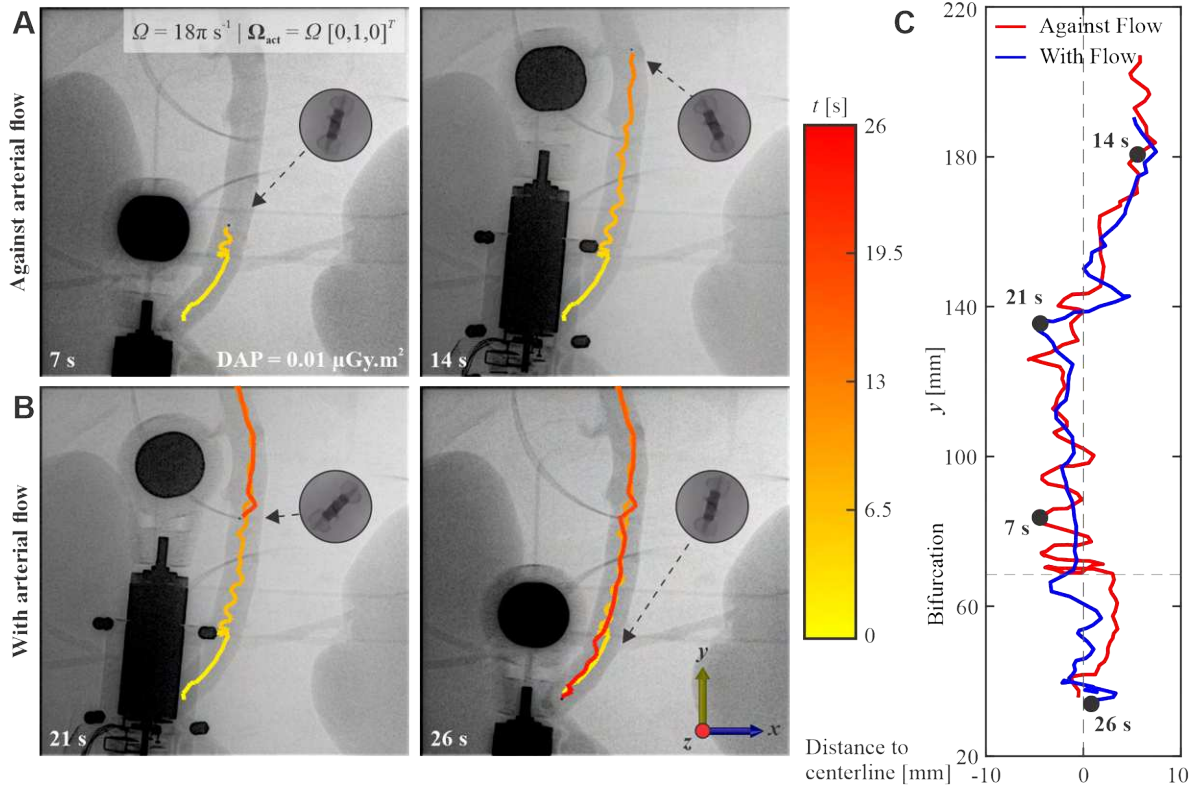


**Fig. 5.** The UMR is directed in a controlled manner both against and with the direction of arterial flow, maintaining movement below its step-out frequency. The UMR is actuated against (A) and with (B) arterial flow at actuation frequency of 9 Hz. (C) The UMR exhibits greater lateral displacement when swimming against the flow (movie S2).

Fig. 4E presents the projected UMR swimming speed as a function of the normalized wavenumber  $\nu$  and cylinder-to-vessel ratio  $R_{\text{cyl}}/R_{\text{vec}}$ . Smaller normalized wavenumber values correspond to increased speed. Both the 9-mm-long UMR and the 12-mm-long UMR exhibit an average normalized wavenumber of approximately 2.2. In narrower vessels, there is an observed speed increase compared to wider vessels. Consequently, higher speeds are anticipated in the renal artery compared to the aorta. In the aorta, the small and large UMRs possess cylinder-to-vessel ratios of 0.32 and 0.42, resulting in predicted speeds of 6 mm/s and 12 mm/s, respectively. Conversely, in the renal artery, the small and large UMR feature cylinder-to-vessel ratios of 0.56 and 0.75, leading to predicted speeds of 18 mm/s and 74 mm/s, respectively.

We compare the observed swimming speeds when the UMRs are allowed to move both against and with the blood flow. Straight runs of the UMR along the abdominal aorta of the *ex vivo* model are conducted at actuation frequencies below the step-out threshold, aiming to achieve maximum propulsive thrust. Figure 5 illustrates the trajectory taken by the same 12-mm-long UMR during a straight run at actuation frequency of 9 Hz. In this trial, the run begins by propelling the UMR against the flow, originating from the distal end of the abdominal aorta and progressing toward its proximal end. As the UMR moves along its path, it encounters varying flow velocities. Notably, the blood flow speed past the bifurcation of the renal arteries exceeds that of any other parts of the *ex vivo* model. Consequently, at  $t = 5$  s, a noticeable disparity in the UMR's trajectory emerges. The presence of the renal circulation leads to a reduction in blood flow past the bifurcation, and as the UMR advances beyond this location, it encounters greater arterial flow. Once the UMR reaches the renal bifurcation, its previously smooth trajectory transforms into a zigzag curve, resulting in increased horizontal displacement and, on average, a decrease in swimming speed (Fig. 5A). Alternatively, when the UMR is allowed to swim with the flow (as indicated by the blue trajectories), its propulsive thrust aligns with the direction of the flow, resulting in more seamless swimming behavior, as shown in Fig. 5B. In Fig. 5C, the graph displays the measured distance between the UMR and the centerline of the aorta during this straight-run. The UMR exhibits greater lateral displacement when swimming against the flow, especially when it swims closer to the centerline of the aorta where the flow velocity is higher. On the other hand, when the motion is reversed and the UMR swims with the flow, it becomes more oriented toward the centerline due to the velocity gradient within the aorta.

We gradually increase the blood flow and evaluate the straight-run performance of the UMRs both against and with the arterial flow, as shown in Figure 6 and movie S2. The measured swimming speed of the UMR against the flow exhibits a seemingly linear trend, with the

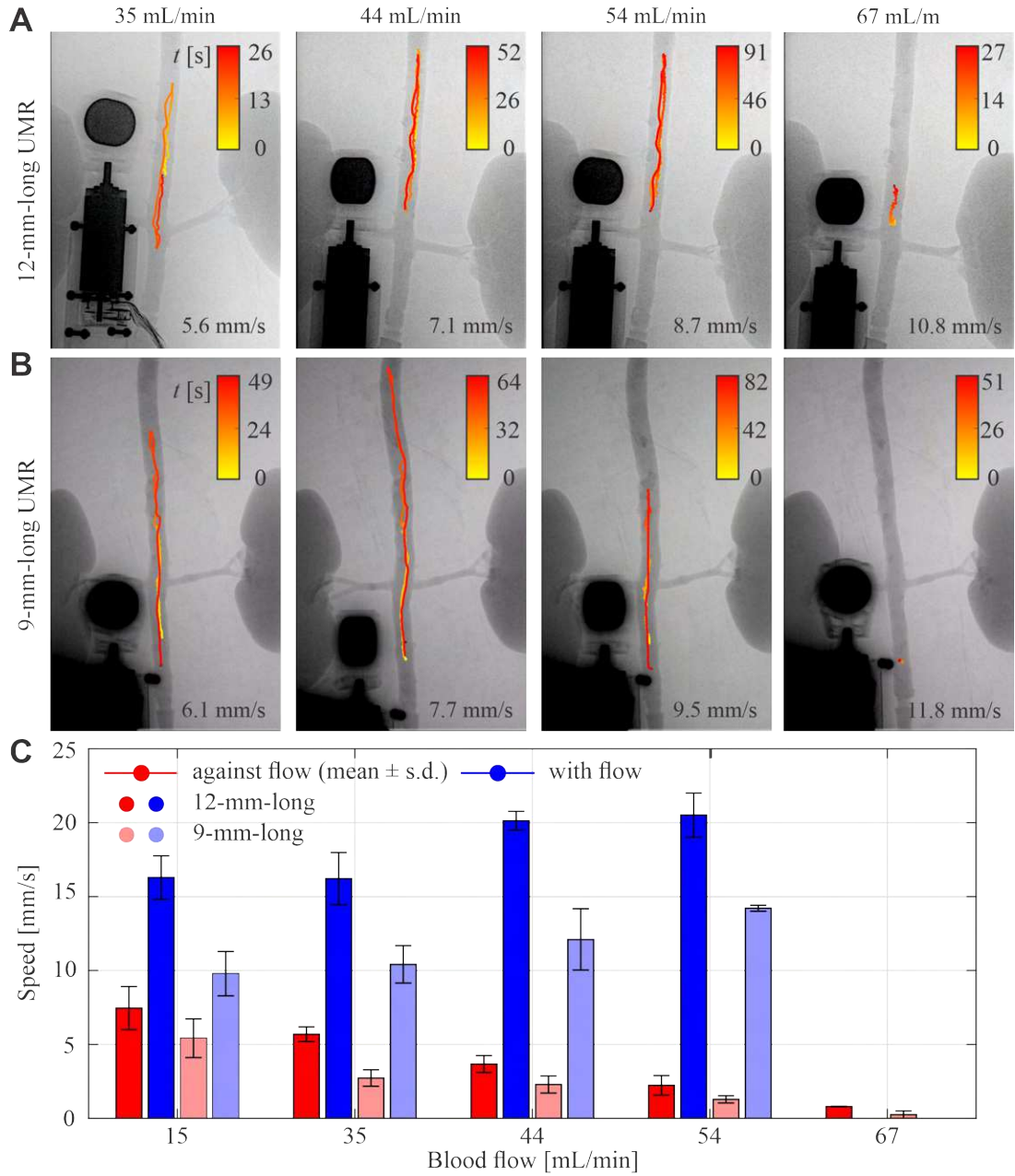


**Fig. 6. The swimming velocity of the UMRs is assessed within the range of blood flow rates from 15 to 67 mL/min.** (A)-(B) To achieve consecutive straight-runs at an actuation frequency of 9 Hz for each flow rate, the UMR is moved under controlled maneuver. The average speeds are determined based on data collected from five separate trials. (C) The robotic platform effectively maintains the UMR's position against the highest blood flow rate of 67 mL/min (movie S2).

speed decreasing as the flow increases. At a flow rate of 67 mL/hr, the propulsive thrust proves adequate to counteract the flow, although resulting in a small net displacement. In contrast, swimming with the flow results in a speed increase, yet still demonstrates a qualitative correlation with blood flow. A plug flow model aligns well with flow rates exceeding 15 mL/min, where the calculated speed,  $U$ , falls within the range of 16 – 19 mm/s, under a 9 Hz actuation frequency of the UMR. These values are depicted in Fig. 4. Additionally, a friction factor ranging from 0.8 – 1.4 for small UMR and 0.4 to 0.74 for large UMR estimates a reduction in the UMR’s speed attributed to friction with the vessel wall (aorta). In the renal artery, the friction coefficient of the small UMR increased to 1.6 indicating a higher friction due to narrower vessel. The swimming speed with flow displays a trend that seems to be less responsive to variations in blood flow. With the UMR and the RPM magnetically interconnected, the field gradient will likely induce a pulling force in the opposite direction of the flow.

## **Directional control and steering maneuver into the renal artery**

Guided by the motion characteristics and theoretical model of the UMR, we control the UMR toward the left renal artery to showcase its navigational capabilities. Controlling the magnetic fields is achieved by employing a position-controlled RPM-actuator configured in a manner that enables direct teleoperation of its rotation axis,  $\Omega_{\text{act}}$ , and position. Visual tracking of the UMR is facilitated through X-ray Fluoroscopy images captured at a fluoroscopy dose rate of  $0.62 \text{ mGy}\cdot\text{cm}^2\text{s}^{-1}$  (refer to Methods). Radiation exposure is monitored throughout each trial, ensuring a reduction in the overall radiation dosage, leading to relatively low contrast resolution.

The UMR’s passage into the left renal artery along renal flow is achieved through several stages: an initial swimming maneuver toward the renal artery’s bifurcation (aligned along the  $\pm y$ -axis within the reference frame of Figure 7A), a subsequent turning maneuver toward the entry point of the renal artery, followed by a rolling maneuver along the  $\pm y$ -axis, and ulti-

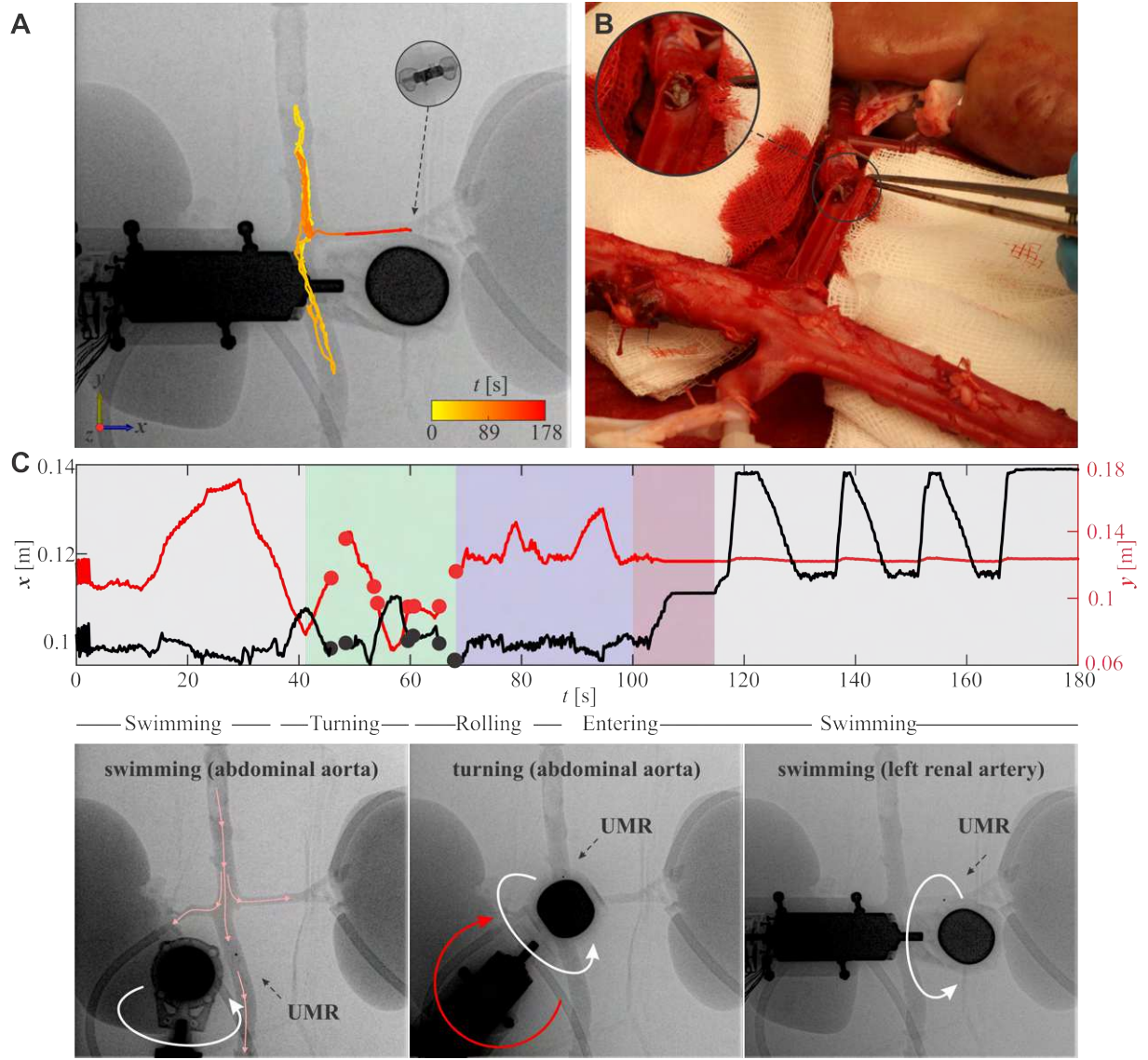


**Fig. 7. The UMR is remotely operated to navigate through the abdominal aorta, engaging in a series of straight runs before executing a turning maneuver within the left renal artery. (A) The RPM-actuator is teleoperated to exert in-plane torque required to steer the UMR toward the left renal artery. (B) The UMR is extracted from the left renal artery and no damage in the wall lining is observed. (C) A four-stage sequence is executed to transition the UMR from its location in the abdominal aorta to the renal artery. The small circles on the visual representation denote instances where the visual feedback of the UMR is obscured by the RPM-actuator.**

mately a swimming maneuver with the renal flow along the  $\pm x$ -axis (Movie S1 and S3). This four-stage sequence is adopted due to the near right angle formed by the renal artery and the abdominal aorta, making a direct turn substantially challenging. Additionally, due to the inherent limitations of 2D X-ray Fluoroscopy image acquisition, accurately determining the UMR's depth within the abdominal aorta is unfeasible. This, in turn, hinders the ability to make precise adjustments to its height in relation to the entry point of the renal artery using out-of-plane pitch angle swimming.

Screw-shaped UMRs are adept at maneuvering and rolling in proximity to any wall. By rotating the UMR by  $90^\circ$  about the  $z$ -axis, its long axis becomes perpendicular to the abdominal aorta and aligned with the left renal artery. Consequently, alternating rolling motions around the entry point for roughly 30 seconds results in successful entry. This rolling is succeeded by swimming and sequential motion reversals within the renal artery. In this trial, teleoperation guides the UMR to the distal end of the left renal artery in less than 180 seconds. Furthermore, upon internal wall inspection, we observe no indications of damage (as depicted in Fig. 7B).

Fig. 7C depicts the sequence of teleoperated inputs that guide the UMR from the abdominal artery to the distal end of the left renal artery. Between  $0 < t < 40$  seconds, the UMR initiates swimming against the blood flow along the  $+y$ -axis, moving past the renal bifurcation. Around  $t \sim 30$  seconds, the UMR's direction is reversed, and it is directed to swim again toward the renal bifurcation along the  $-y$ -axis, following the flow. Upon passing the renal bifurcation, the swimming direction is reversed again and the RPM is gradually turned about the  $z$ -axis to exert an in-plane torque, steering the UMR parallel to the renal artery. Multiple overlaps between the RPM and the UMR obstruct visual feedback during this turning maneuver. This is clearly indicated by the small circles in Fig. 7C between  $40 < t < 65$  seconds. Subsequently, the UMR is controlled to roll back and forth between  $65 < t < 110$  seconds to enter the left renal artery, assisted by the renal flow.



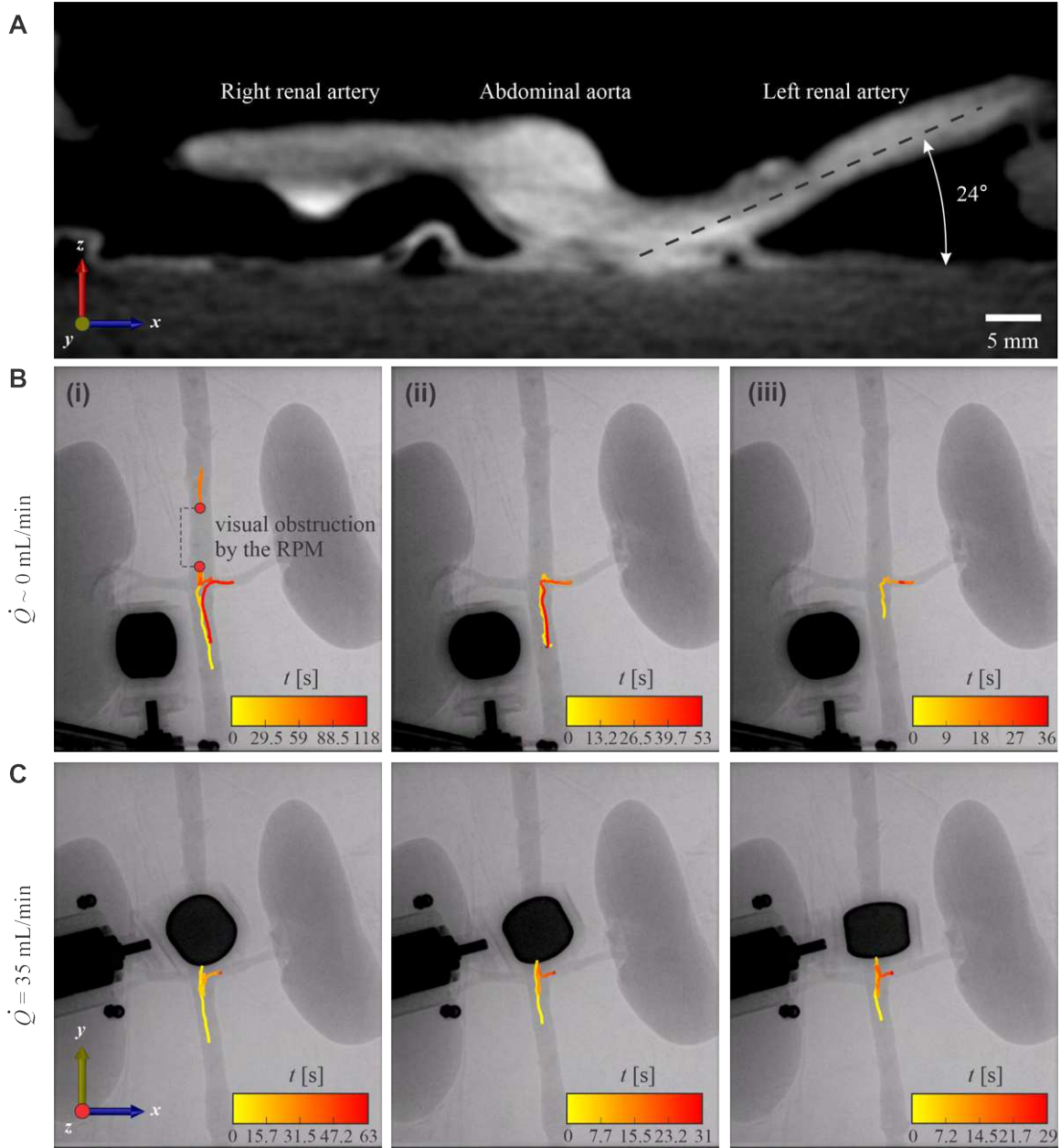


**Fig. 8. The 9-mm long UMR is controllably moved back and forth between the abdominal aorta and the proximal end of the left renal artery. (A)** A CBCT-scan shows the  $xz$ -plan of the renal bifurcation. **(B)** Motion control is achieved in a stationary blood flow ( $\dot{Q} \sim 0$ ). **(C)** Motion control is achieved in blood flow of 35 mL/min.

Once inside the renal artery (around  $t \sim 115$  seconds), the UMR swims toward its distal end at a faster speed than that in the abdominal artery. Similarly, when the swimming direction

inside the renal artery is reversed (around  $t \sim 125$  seconds) and the UMR swims back toward the entry point, its speed exceeds that against the arterial flow. This motion enhancement is attributed to the wall effect. With the smaller diameter inside the renal artery, the flow provides an extra force on the body, which increases the swimming speed.

Figure 8A presents a cross-section view of the renal bifurcation obtained through a CBCT-scan. Clearly, the centerline of the abdominal aorta does not align with the horizontal planes of either the left or the right renal arteries. The left renal artery exhibits a  $24^\circ$  inclination with respect to the horizontal  $xy$ -plane. Nevertheless, it remains feasible to guide the UMR toward the entry point of the left renal artery and subsequently return to the abdominal aorta. Fig. 8(B) and movie S4 show three consecutive motion control trials directed toward the left renal artery under conditions of stationary blood flow. Throughout these trials, the operator effectively maintained synchronization between the UMR and the RPM, even when faced with temporary visual obstructions (Fig. 8B(i)). To mitigate such visual obstructions, adjusting the UMR's trajectory to enable a direct entry into the left renal artery, as demonstrated in Figs. 8B(ii) and 8B(iii), can prove to be a highly effective strategy. Direct turns like these are achievable under stationary fluid conditions or with very low flow rates. However, as the flow rate increases, executing a direct  $90^\circ$  turn becomes challenging. In such cases, we employ a combination of rolling and swimming to access the renal artery in less than 60 seconds, as demonstrated in three representative trials in Fig. 8C and movie S4.

## DISCUSSION

In this study, we demonstrate the feasibility of biocompatible UMRs, which are actuated by X-ray-guided magnetic fields. We conduct an in-depth analysis of the UMRs' response using magneto-hydrodynamic models, which serves as a basis for selecting design parameters and control inputs for motion control within an *ex vivo* porcine aorta model. For UMRs that display

a small normalized wavenumber (large normalized helical pitch), the cylinder-to-vessel ratio significantly impacts their swimming speed. Conversely, as the normalized wavenumber increases, the influence of confinement diminishes. Based on these theoretical predictions, several design concepts can be proposed to address navigation challenges within varying blood-vessel diameters. The first design involves screw-shaped bodies with relatively small normalized helical pitch (large wavenumbers), resulting in slower locomotion but reduced sensitivity to the diameter of the confinement. A second design features screw-shaped bodies with relatively high helical pitches (small normalized wavenumber), which enhances swimming speed as the cylinder-to-vessel ratio increases, making them well-suited for narrower vessels. Our design blends the robustness of the first type in response to varying blood-vessel diameters with the propulsion enhancement anticipated with the low helical pitch and increasing cylinder-to-vessel ratio of the second type. With this level of control and based on our theoretical predictions, we demonstrate successful direct teleoperation of 9-mm-long UMRs within the abdominal aorta, advancing toward the distal end of the renal artery.

The swimming speeds of our UMRs demonstrate remarkable efficiency, comparable to tethered catheters. It is crucial to emphasize that in medical procedures, clinicians typically have control over the speed at which a catheter is advanced or withdrawn, allowing for adjustments as needed for the specific procedure. When scaled by their body length, our 12-mm-long and 9-mm-long UMRs achieve maximum swimming speeds of 1.6 and 3.3 body lengths per second below their step-out frequencies, respectively. The enhanced efficiency of the smaller UMR is mainly enabled by its reduced resistance to rotation, a characteristic that scales as  $R_{\text{cyl}}^2$ , resulting in a swimming speed that increases linearly with rotational speed  $\omega$  and  $R_{\text{cyl}}$ . This scaling effect highlights the advantages of smaller UMRs in achieving higher relative speeds, comparable to those achieved by tethered devices when controlled by clinicians. However, it is worth noting that catheters have the advantage of exerting much greater force, making them effective

for engaging with, for example, thrombus. Currently, our UMRs efficiently harvest magnetic energy and transduce it entirely into work to reach the desired site. Achieving comparable engagements with thrombus as catheters may require significantly greater force. To enhance the frequency response and propulsive thrust of our UMRs, we can explore increasing their magnetic moment and enhancing the strength of the actuating field, which could further improve their performance in targeted applications.

## **MATERIALS AND METHODS**

### ***Ex vivo* model**

Porcine retroperitoneal organs, including the abdominal aorta and kidneys, along with blood, were procured from a slaughterhouse. Following the standard practice for meat processing, the pigs (*Sus scrofa domesticus*, the Netherlands) were rendered unconscious with an electric current applied through electrodes on the body. Subsequently, the carotid artery was incised to drain the animals of blood. The collected blood was directly obtained from the carotid artery wound and placed in a plastic container prepped with 1000 IE heparin per liter of blood (Leo Pharma, Ballerup, Denmark). A total of ten liters of blood was collected from multiple pigs for a single experiment. The retroperitoneal organs, including the aorta and kidneys along with attached soft tissues, were excised and immediately placed in a plastic bag on ice for transport to the operating room (OR). During transport, the blood was kept at room temperature.

In the OR, the abdominal aorta, renal vessels, and kidneys were isolated. All aortic side branches, except the renal arteries, were ligated. A standard roller pump perfusion system employing a disposable set for extracorporeal organ perfusion was utilized. An overflow-secured reservoir was interposed between the pump and the aorta. The system was primed with the heparinized blood. The aorta, with the attached kidneys, was positioned on a plastic sheet and connected to the perfusion setup by cannulating the proximal and distal aorta. The distal renal

arteries were also cannulated and linked to the flow system to ensure flow within both renal arteries, while minimizing blood loss through the renal veins. The blood flow was measured to allow experiments at varying flow rates.

### ***In vitro* tissue and vessel phantom**

We conducted prolonged experiments, including characterizing the frequency response in blood, using an *in vitro* tissue and vessel phantom. Developing the phantom (275 mm×85 mm×40 mm) involved employing a three-piece mold. Initially, the muscle edge layer was positioned on the base plate, and within the muscle edge, vessels (artery: Rehau Silicone 3/8" × 3/32"; vein: Rehau Silicone 3/16" × 1/16") and a femoral nerve (silicone round cord: Ø5 mm), each measuring 350 mm in length, were inserted. To mimic the femoral sheath, an interfacing tissue (80×50 mm) was enveloped around the vein and artery, temporarily secured using a paperclip. Following exposure to a heat gun, the paperclip could be detached, allowing the overlapping sides of the tissue to rotate downwards. Mimicking muscle tissue required preparing Ecoflex™ 00-30 with Silc Pig™ Blood pigment, utilizing a WASSERMAN Wamix Touch vacuum mixer. After the curing process, the fat edge layer was added on top of the preceding edge. To mimic fat tissue, Soma Foama™ 15 silicone with Silc Pig™ blood and Silc Pig™ white pigment was prepared using a hand mixer. Following another curing step, the skin edge layer was superimposed onto the previous edge. Subsequently, to replicate skin tissue, Ecoflex™ 00-30 with Silc Pig™ flesh tone was prepared using a WASSERMAN Wamix Touch vacuum mixer. Upon completing the final curing period, the entire mold was extracted.

### **Design of the UMRs**

The UMRs were designed using three-dimensional computer-aided design software (SolidWorks, Dassault Systèmes, SolidWorks Corp. Inc., USA). The design consists of two identical

halves which are joint together while enclosing a permanent magnet. The design finds its origin in previous research where they demonstrated blood clot removal (39). The length and diameter of the UMRs are based on the inner diameters of the abdominal artery and renal artery respectively (table S1), the used parameters can be found in Table S2.

## **Fabrication of the UMRs**

The UMRs were produced through Masked Stereolithography Apparatus (MSLA) employing a 3D printer (Phrozen Sonic Mini 4K). Phrozen Aqua-Gray 4K resin was the chosen material. During printing, a single layer height of 50  $\mu\text{m}$  was utilized. Subsequent to printing, the components underwent cleaning with isopropyl alcohol (IPA) in an ultrasonic bath for a duration of 7 minutes. Post-curing was carried out using an Elegoo Mercury plus curing station for a duration of 12 minutes. After curing, UMRs were coated with LipoCoat 4AC coating technology by manual dipcoating for 10 s. Coated UMRs were, then, left to dry overnight under ambient conditions in the dark.

UMRs, possessing a minimum length ( $L$ ) and diameter 9 mm and 3.75 mm respectively, were constructed by assembling a 3D-printed screw-shaped body with an enclosed permanent magnet composed of NdBFe Grade-N45 material (S-01-01-N Supermagnete, Gottmadingen, Germany). The permanent magnet is cylindrical with axial magnetization, measuring 1 mm in diameter and 1 mm in length, with a magnetic moment ( $m$ ) of  $8.4 \times 10^{-4} \text{ A} \cdot \text{m}^2$ . The permanent magnet was positioned such that its magnetic moment was perpendicular to the long axis of the screw-shaped body. This configuration enabled the UMR to swim within blood upon rotation and follow an external weak-strength magnetic field of 5 mT.

## Coating characterization

The successful coating application of UMR material was assessed by comparing coated material to uncoated controls with regard to their water contact angle (CA) using a Krüss DSA30S and to their fluorescence intensity of a fluorescently-labeled coating variant (using an Echo Revolve 4M). Results shown in the SI (Fig. S1) prove the successful coating application.

Furthermore, several biocompatibility tests were carried out on coated UMR- and other materials. Protein fouling was tested using a fluorescently-labeled fibrinogen variant. Briefly, coated and uncoated UMR material was incubated in PBS containing 0.1 mg/mL fibrinogen-A647 for 2 h at 37°C without agitation. After washing in de-ionized water (MQ), samples were transferred to fresh phosphate buffered saline for imaging. Average intensities of fibrinogen-A647 adsorbed to coated and uncoated samples were determined using ImageJ (43) and are shown in Fig. 2I.

Biofilm formation was tested on coated, compared to uncoated, PU catheter material using a commercially available *Staphylococcus aureus* strain (ATCC 25923). Briefly, an overnight culture of *S.a.* from Lysogeny broth was washed with M9 minimal salt medium containing 0.4% glucose and 1 mM MgSO<sub>4</sub>. Coated and uncoated samples were incubated for 72 h at 37°C without agitation in the washed o/n culture, diluted with M9 to  $OD_{600}$  0.03. Subsequently, samples were gently washed three times with MQ, fixed by submersion in 4% paraformaldehyde for 10 min, washed with MQ, stained by submersion for 15 min in 3 µg/mL propidium iodide, washed three times with MQ and imaged dry using a fluorescence microscope. Average intensities of propidium iodide-stained *S.a.* attached to coated and uncoated samples were determined using ImageJ (?) and are shown in Fig. 2J.

A fibrin generation test was carried out in the presence of coated and uncoated UMR material. Briefly, platelet poor plasma (PPP) was isolated from freshly drawn, citrated whole-blood (35). Samples were immersed in 65% PPP in 0.9% NaCl, pre-heated to 37°C, and re-

initiated by adding 100 mM  $\text{CaCl}_2$  (also pre-heated) to reach a final concentration of 14 mM. Immediately after re-initiation, the scatter signal at  $A_{405}$  was monitored for 1 h using a Tecan Infinite 200 Pro M Plex. The resulting time traces and a box plot of their inflection points are shown in Fig. 2K.

## Fluidic and structural effects

The UMR is a screw-shaped rigid body with a length of  $L$ , a diameter of  $D$ , and an average magnetic moment  $\mathbf{m}$  oriented perpendicular to its long axis. Fluid velocity, vessel walls, and fluid flow within the vessels influence the velocity of the UMR. The body is mathematically represented as a helical wave superimposed onto a cylinder with a radius of  $R_{\text{cyl}}$ , and its surface is described by:

$$\mathbf{x}(\theta, \zeta) = \rho(\theta) [\cos(\nu^* \zeta + \theta) \hat{\mathbf{x}} + \sin(\nu^* \zeta + \theta) \hat{\mathbf{y}}] + \zeta \hat{\mathbf{z}}, \quad (1)$$

where  $\theta \in [0, 2\pi)$  and  $\zeta \in (-\infty, \infty)$  are helical coordinates and the function  $\rho(\theta) = R_{\text{cyl}}[1 + \epsilon f(N\theta)]$  describes the profile of the cross-section of the screw-shaped body, and  $f(N\theta) = \sin(N\theta)$  is a periodic function,  $N$  and  $\epsilon$  are the number and the amplitude of starts of the screw. When the UMR submerged in blood is subject to an external magnetic torque,  $\mathbf{T} = \mathbf{m} \times \mathbf{B}$ , it will move with velocity  $U$  and angular rotational rate,  $\omega$ , satisfying

$$U = 2R_{\text{cyl}}\omega\epsilon^2 \sum_{q \geq 1} \frac{(1 + \beta q^2 De^2) |\hat{f}_q|^2}{1 + q^2 De^2} J_q, \quad (2)$$

where  $De = \tau\omega$  is the Deborah number,  $\tau$  is the fluid relaxation timescale, and  $\beta = \eta_s/\eta$  is a ratio of the blood serum viscosity to the total viscosity of blood (38, 41). The fluid relaxation timescale is estimated from oscillatory shear experiments as

$$\tau = \lim_{\omega \rightarrow 0} \frac{G'}{\omega G''}. \quad (3)$$

Here the real and imaginary parts of the complex elastic modulus denoted as  $G'$  and  $G''$ , respectively. In the case of blood, the Deborah number is typically  $De = 0.1$  (42). The viscosity of



blood serum is approximately  $1.4 - 1.5 \text{ mPa}\cdot\text{s}$ , resulting in a value of  $\beta = 0.43$  for blood and  $\beta = 0.0015$  for blood clot.

The determination of translational velocity for UMRs within vessels of radius  $R_{\text{ves}}$  is carried out by distributing Stokeslet points on both the screw-shaped rigid body and the cylindrical vessel surface (44). Stokeslet points on the screw-shaped rigid body are positioned according to Equation 1 for a total of two turns. These points on the UMR surface possess a velocity of  $v(\theta, \zeta) = \omega \times x + U_N$ . Meanwhile, the Stokeslet points on the vessel surface remain at a zero velocity. Subsequently, forces acting on the Stokeslet points are computed, ultimately leading to the determination of the total force acting on the UMR. The translational velocity along the capillary is adjusted until the net force on the UMR reaches zero. This velocity is then determined for various wavenumbers  $\nu^*$  and cylinder-to-vessel ratio  $R_{\text{cyl}}/R_{\text{ves}}$ . The utilized UMRs have an  $\epsilon$  value of 0.33 and a normalized wavenumber of  $\nu = R_{\text{cyl}}\nu^* = 2.2$ . The  $R_{\text{cyl}}/R_{\text{ves}}$  ratio varies with specific UMR applications: The ratio is 0.42 for large UMRs within the aorta, 0.75 for large UMRs in arteries, 0.32 for small UMRs within the aorta, and 0.56 for small UMRs in arteries.

When the UMR moves through a vessel with a flow rate, a plug flow relation is assumed, denoted as  $\dot{Q} = \pi R_{\text{ves}}^2 U_f$ , between the flow rate  $\dot{Q}$  and the fluid flow velocity  $U_f$ . The UMR's velocity with the flow is given by  $U_w = U + U_f - cU_w$ , and against the flow, it is  $U_a = U - U_f - cU_a$ . Here,  $U$  represents the UMR velocity in the absence of flow,  $cU$  accounts for the friction between the UMR and the vessel wall, and  $c$  is the friction coefficient. The friction coefficient  $c$  and velocity  $U$  can be determined as follows:  $f$  is calculated as  $c = (2U_f/(U_w - U_a)) - 1$ , and  $U$  is determined as  $U = (c + 1)(U_w + U_a)/2$ .

## Wireless manipulation setup

Wireless actuation is achieved through a robotically controlled RPM-actuator. The mechanism generates a rotating magnetic field utilizing a cylinder crafted from NdBF<sub>e</sub> Grade-N45 material, measuring 35 mm in diameter and 20 mm in height, featuring a magnetic moment of 18.89 A·m<sup>2</sup>. The rotational velocity of the permanent magnet is managed using a Maxon 18 V brushless DC motor, while its orientation is regulated via a KUKA 6-DOF manipulator (KUKA KR-10 1100-2, KUKA, Augsburg, Germany). This wireless manipulation carried out within a C-Arm fluoroscopic room. The operator is positioned behind a mobile lead barrier for radiation protection, facilitating robotic movement of the RPM.

## Ultrasound imaging

The frequency response of the UMRs in blood was determined by assessing the swimming speed using ultrasound images. For this purpose, the UMRs were placed within the vessel of the *in vitro* phantom model, characterized by a diameter of 9.5 mm. A 14L5 ultrasound transducer was securely positioned beneath the phantom model, emitting ultrasound waves at a frequency of 11 MHz. A series of consecutive straight runs of the UMR were conducted ( $n = 6$ ) for each actuation frequency of the RPM. The shading displayed in Fig. 4C illustrates the standard deviation (s.d.) in the results.

## Fluoroscopy and Cone Beam CT images

The dimensions of the vessels are extracted from a Cone Beam CT scanner, obtained from three distinct *ex vivo* animal models. In the teleoperation trials, X-ray Fluoroscopy images are captured utilizing the Siemens Healthineers Artis Pheno (Erlangen, Germany). The image acquisition transpires at a frame rate of 5 Hz, with an X-ray voltage peak of 56.9 kV, tube current of 120 mA. Throughout the trials, no additional contrast media are introduced, barring

one *in vitro* trial (insets in Fig. 3A) where the intention is to depict the UMR's geometry. The wireless actuation employs X-ray Fluoroscopy images deliberately generated with low contrast resolution. This is executed to demonstrate the capability to control the UMR using minimal radiation doses.

## REFERENCES AND NOTES

1. B. J. Nelson, I. K. Kaliakatsos, J. J. Abbott, "Microrobots for minimally invasive medicine," *Annual Review of Biomedical Engineering*, vol. 12, no. 1, pp. 55–85, 2010.
2. M. Sitti, H. Ceylan, W. Hu, J. Giltinan, M. Turan, S. Yim, E. Diller, "Biomedical applications of untethered mobile milli/microrobots," *Proceedings of the IEEE*, vol. 103, no. 2, pp. 205–224, 2015.
3. L. Ricotti, B. Trimmer, A. W. Feinberg, R. Raman, K. K. Parker, R. Bashir, M. Sitti, S. Martel, P. Dario, A. Menciassi, "Biohybrid actuators for robotics: A review of devices actuated by living cells," *Science Robotics*, vol. 2, no. 12, 2017.
4. O. Felfoul, M. Mohammadi, S. Taherkhani, et al. "Magneto-aerotactic bacteria deliver drug-containing nanoliposomes to tumour hypoxic regions," *Nature Nanotechnology*, vol. 11, 941–947, 2016.
5. T. Xu, J. Zhang, M. Salehizadeh, O. Onaizah, E. Diller, "Millimeter-scale flexible robots with programmable three-dimensional magnetization and motions," *Science Robotics*, vol. 4, 2019.
6. M. Medina-Sánchez, L. Schwarz, A. K. Meyer, F. Hebenstreit, O. G. Schmidt, "Cellular cargo delivery: Toward assisted fertilization by sperm-carrying micromotors" *Nano Letters*, vol. 16, 1, 555–561, 2016.

7. F. Rajabasadi, S. Moreno, K. Fichna, A. Aziz, D. Appelhans, O. G. Schmidt, M. Medina-Sánchez, “Multifunctional 4D-Printed sperm-hybrid microcarriers for assisted reproduction,” *Advanced Materials*, vol. 34, no. 50, 2022.
8. S. Martel and M. Mohammadi, “Using a swarm of self-propelled natural microrobots in the form of flagellated bacteria to perform complex microassembly tasks,” in *IEEE International Conference on Robotics and Automation (ICRA)*, pp. 500–505, 2010.
9. F. N. P. Basualdo, A. Bolopion, M. Gauthier, P. Lambert, “A microrobotic platform actuated by thermocapillary flows for manipulation at the air-water interface,” *Science Robotics*, vol. 6, 2021.
10. F. Carpi and C. Pappone, “Magnetic maneuvering of endoscopic capsules by means of a robotic navigation system,” in *IEEE Transactions on Biomedical Engineering*, vol. 56, no. 5, pp. 1482-1490, 2009.
11. S. Taherkhani, M. Mohammadi, J. Daoud, S. Martel, M. Tabrizian, “Covalent binding of nanoliposomes to the surface of magnetotactic bacteria for the synthesis of self-propelled therapeutic agents,” *ACS Nano*, vol. 27, no. 8(5), pp. 5049-60, 2014.
12. Q. Wang, J. Zhang, J. Yu, J. Lang, Z. Lyu, Y. Chen, L. Zhang, “Untethered small-scale machines for microrobotic manipulation: from individual and multiple to collective machines,” *ACS Nano*, 2023.
13. A. W. Mahoney and J. J. Abbott, “Generating rotating magnetic fields with a single permanent magnet for propulsion of untethered magnetic devices in a lumen,” *IEEE Transactions on Robotics*, vol. 30, no. 2, pp. 411-420, 2014.
14. R. Dreyfus, J. Baudry, M. L. Roper, M. Fermigier, H. A. Stone, J. Bibette, “Microscopic artificial swimmers,” *Nature*, 437, 862-865, 2005.

15. L. Zhang, J. J. Abbott, L. Dong, B. E. Kratochvil, D. Bell, B. J. Nelson, "Artificial bacterial flagella: fabrication and magnetic control," *Applied Physics Letters*, vol. 94, no. 6, pp. 064107, 2009.
16. F. Bianchi, A. Masaracchia, E. S. Barjuei, A. Menciassi, A. Arezzo, A. Koulaouzidis, D. Stoyanov, P. Dario, G. Ciuti, "Localization strategies for robotic endoscopic capsules: a review," *Expert Review of Medical Devices*, vol. 16, no. 5, pp. 381-403, 2019.
17. A. Aziz, S. Pane, V. Iacovacci, N. Koukourakis, J. Czarske, A. Menciassi, M. M. Sánchez, O. G. Schmidt, "Medical imaging of microrobots: Toward in vivo applications," *ACS Nano*, vol. 14, no. 9, pp. 10865-10893, 2020.
18. J. Jiang, Z. Yang, A. Ferreira, L. Zhang, "Control and autonomy of microrobots: recent progress and perspective," *Advanced Intelligent Systems*, vol. 4, no. 5, 2022.
19. X. Yan, Q. Zhou, M. Vincent, Y. Deng, J. Yu, J. Xu, T. Xu, T. Tang, L. Bian, Y.-X. J. Wang, K. Kostarelos, Li Zhang, "Multifunctional biohybrid magnetite microrobots for imaging-guided therapy," *Science Robotics*, vol. 2, no. 12, 2017.
20. D. Jin, Q. Wang, K. F. Chan, N. Xia, H. Yang, Q. Wang, S. C. H. Yu, L. Zhang, "Swarming self-adhesive microgels enabled aneurysm on-demand embolization in physiological blood flow," *Science Advances*, vol. 9, no. 6, 2009.
21. A. Ghosh and P. Fischer, "Controlled propulsion of artificial magnetic nanostructured propellers," *Nano Letters*, vol. 9, no. 6, 2009.
22. X. Wang, X.-H. Qin, C. Hu, A. Terzopoulou, X.-Z. Chen, T.-Y. Huang, K. Maniura-Weber, S. Pané, Bradley J. Nelson, "3D Printed enzymatically biodegradable soft helical microswimmers," *Advanced Functional Materials*, vol. 28, no. 45, 2018.

23. H. Ceylan, I. Ceren Yasa, O. Yasa, A. F. Tabak, J. Giltinan, M. Sitti, “3D-Printed biodegradable microswimmer for theranostic cargo delivery and release,” *ACS Nano*, vol. 13, no. 3, 2019.
24. A.C. Bakenecker, A. von Gladiss, H. Schwenke, et al. “Navigation of a magnetic micro-robot through a cerebral aneurysm phantom with magnetic particle imaging,” *Scientific Reports*, vol. 11, no. 14082, 2021.
25. E. E. Niedert, C. Bi, G. Adam, E. Lambert, L. Solorio, C. J. Goergen, D. J. Cappelleri, “A tumbling magnetic microrobot system for biomedical applications,” *Micromachines*, vol. 11, no. 9, 2020.
26. M. Vonthron, V. Lalande, G. Bringout, C. Tremblay, S. Martel, “A MRI-Based integrated platform for the navigation of microdevices and microrobots”, in *Proc. IEEE J. Int. Conf. Intell. Robots Syst.*, pp. 1285-1290, 2011.
27. M. E. Tiryaki, F. Doğangün, C. B. Dayan, P. Wrede, M. Sitti, “MRI-Powered magnetic miniature capsule robot with HIFU-controlled on-demand drug delivery,” in *IEEE International Conference on Robotics and Automation (ICRA)*, London, United Kingdom, 2023, pp. 5420-5425.
28. A. Servant, F. Qiu, M. Mazza, K. Kostarelos, B. J. Nelson, “Controlled in vivo swimming of a swarm of bacteria-like microrobotic flagella”, *Advanced Materials*, vol. 27, no. 19, pp. 2981-2988, 2015.
29. G. Koçer and P. Jonkheijm, “About chemical strategies to fabricate cell-instructive biointerfaces with static and dynamic complexity,” *Advanced Healthcare Materials*, vol. 7, pp. 1701192, 2018.

30. G. Koçer and P. Jonkheijm, "Guiding hMSC adhesion and differentiation on supported lipid bilayers," *Advanced Healthcare Materials*, vol. 7, no. 3, 2017.
31. P. Garred, J. Olsen, T. E. Mollnes, T. Bidle, B. E. Glahn, "Biocompatibility of urinary catheters. effect on complement Activation," *British Journal of Urology*, vol. 63, no. 4, 1989.
32. W. van Oeveren, "Obstacles in Haemocompatibility Testing," *Scientifica*, vol. 2013, 2013.
33. P. Eggimann, H. Sax, D. Pittet, "Catheter-related infections. Microbes and infection," *Microbes and Infection*, vol. 6, 2004.
34. M. L. W. Knetsch and L. H. Koole, "New strategies in the development of antimicrobial coatings: The example of increasing usage of silver and silver nanoparticles," *Polymers*, vol. 3, 2011.
35. F. A. W. Coumans, A. R. Brisson, E. I. Buzas, F. Dignat-George, E. E. E. Drees, S. El-Andaloussi, C. Emanuelli, A. Gasecka, A. Hendrix, A. F. Hill, R. Lacroix, Y. Lee, T. G. van Leeuwen, N. Mackman, I. Mäger, J. P. Nolan, E. van der Pol, D. M. Pegtel, S. Sahoo, P. R. M. Siljander, G. Sturk, O. de Wever, R. Nieuwland, "Methodological guidelines to study extracellular vesicles," *Circulation Research*, vol. 120, 2017.
36. M. Hellum, R. Øvstebø, A.-M. S. Trøseid, J. P. Berg, P. Brandtzaeg, C. E. Henriksson, "Microparticle-associated tissue factor activity measured with the Zymuphen MP-TF kit and the calibrated automated thrombogram assay," *Blood Coagul Fibrinolysis*, vol. 23, 2012.

37. K. T. Nguyen et al., "Guide-Wired helical microrobot for percutaneous revascularization in chronic total occlusion in-vivo validation," *IEEE Transactions on Biomedical Engineering*, vol. 68, no. 8, pp. 2490-2498, 2021.
38. L. Li and S. E. Spagnolie, "Swimming and pumping by helical waves in viscous and viscoelastic fluids," *Physics of Fluids*, vol. 27, pp. 021902-1–021902-23, 2015.
39. J. Leclerc, H. Zhao, D. Bao, A. T. Becker, "In Vitro design investigation of a rotating helical magnetic swimmer for combined 3D navigation and blood clot removal," *IEEE Transactions on Robotics*, vol. 36, no. 3, pp. 975-982, 2020.
40. J. Edwards, H. Abdou, N. Patel, M. H. Madurska, K. Poe, J. E. Bonin, M. J. Richmond, T. E. Rasmussen, J. J. Morrison, "The functional vascular anatomy of the swine for research," *Vascular*, vol. 30, no. 2, pp. 392-402, 2022.
41. E. Lauga, "Propulsion in a viscoelastic fluid," *Physics of Fluids*, vol. 19, pp. 083104-1–083104-13, 2007.
42. A. N. Beris, J. S. Horner, S. Jariwala, M. J. Armstrong, N. J. Wagner, "Recent advances in blood rheology: a review," *Soft Matter*, vol. 17, 2021.
43. C.A. Schneider, W. S. Rasband, K.W. Eliceiri, "NIH Image to ImageJ: 25 years of image analysis," *Nature Methods*, vol. 9, 2012.
44. R. Cortez, L. Fauci, A. Medovikov, "The method of regularized Stokeslets in three dimensions: Analysis, validation, and application to helical swimming," *Physics of Fluids*, vol. 17, 2005.



## ACKNOWLEDGMENTS

This work was supported by the Twente University RadBoudumc Opportunities (TURBO) program 2022, Grant Crazy-Research-2022, and EU-DIRNANO programme No. 956544. The authors would like to thank Jaap Greve and Sander Peters for their contributions to the *ex vivo* experimental results.

## Author Contributions

L-J.W.L. conceived and designed the UMRs and the experiments, characterized the motion characteristics of the UMR, analyzed the data, conducted the motion control experiments, and participated in writing and editing of the manuscript. N.R. designed the *in vitro* experiments and characterized the frequency response of the UMR, conducted the motion control experiments. C.G. contributed to the rheological characterization of blood. W.C.D., F.R.H, and J.A. designed and developed of the *in vitro* tissue and vessel phantom. R.L. and M.W. conceived and developed the *ex vivo* porcine aorta model, conducted the control experiments, participated in writing and editing of the manuscript. V.M. participated in the development of the UMRs. A.K. conceived the magneto-hydrodynamic model, and participated in writing and editing of the manuscript. E.A.M.K.R, CH.E.N, D.W., A.S.-A. and P.J. conceived and developed the coating, conducted the biocompatibility experiments, participated in writing and editing the manuscript. H.R.L. supervised the X-ray imaging experiments, participated in the motion control experiments, and contributed to writing and editing the manuscript. I.S.M.K. supervised this work, conceived the experiments, analyzed the data, and participated in writing and editing of the manuscript.

## Competing interests

The authors declare that they have no competing interests.

## Data and materials availability

All data needed to evaluate the conclusions in the paper are present in the paper and/or the Supplementary Materials. Additional data related to this paper may be requested from the corresponding authors via email.

## SUPPLEMENTARY MATERIALS

Fig. S1. Validation of Coating presence on UMR Material.

Fig. S2. UMR velocities in different actuation conditions and branch sizes in *ex vivo* settings.

Table S1. Arteries dimensions of the *ex vivo* models.

Table S2. Design parameters of the UMRs.

Movie S1. Magnetic actuation of a UMR in the Abdominal aorta and left renal artery of an *ex vivo* perfusion model.

Movie S2. UMR swimming trajectories evaluated across a blood flow range of 15 to 67 ml/min in an *ex vivo* abdominal aorta.

Movie S3. UMR locomotion mechanism under the influence of a rotating magnetic field and out-of-plane magnetic torque.

Movie S4. *Ex vivo* navigation of UMRs through the abdominal aorta, including a turning maneuver into the left renal artery.

Supplementary materials for:

## ***Ex vivo* Validation of Magnetically Actuated Intravascular Untethered Robots in a Clinical Setting**

*L.-J. W. Ligtenberg, N. Rabou, C. Goulas, W. C. Duinmeijer, F. R. Halfwerk, J. Arens, R. Lomme, V. Magdanz, A. Klingner, E. A. M. Klein Rot, C. H. E. Nijland, D. Wasserberg, H. R. Liefers, P. Jonkheijm, A. Susarrey-Arce, M. Warlé and I. S. M. Khalil*

### **This file includes:**

Fig S1. Validation of Coating presence on UMR Material.

Fig. S2. UMR velocities in different actuation conditions and branch sizes in *ex vivo* settings.

Table S1. Arteries dimensions of the *ex vivo* models

Table S2. Design parameters of the UMRs

Legends for movies S1 to S4

### **Other supplementary materials for this manuscript:**

Movie S1 (.mp4 format) Magnetic actuation of a UMR in the Abdominal aorta and left renal artery of an *ex vivo* perfusion model.

Movie S2 (.mp4 format) UMR swimming trajectories evaluated across a blood flow range of 15 to 67 ml/min in an *ex vivo* abdominal aorta.

Movie S3 (.mp4 format) UMR locomotion mechanism under the influence of a rotating magnetic field and out-of-plane magnetic torque.

Movie S4 (.mp4 format) *Ex vivo* navigation of UMRs through the abdominal aorta, including a turning maneuver into the left renal artery.

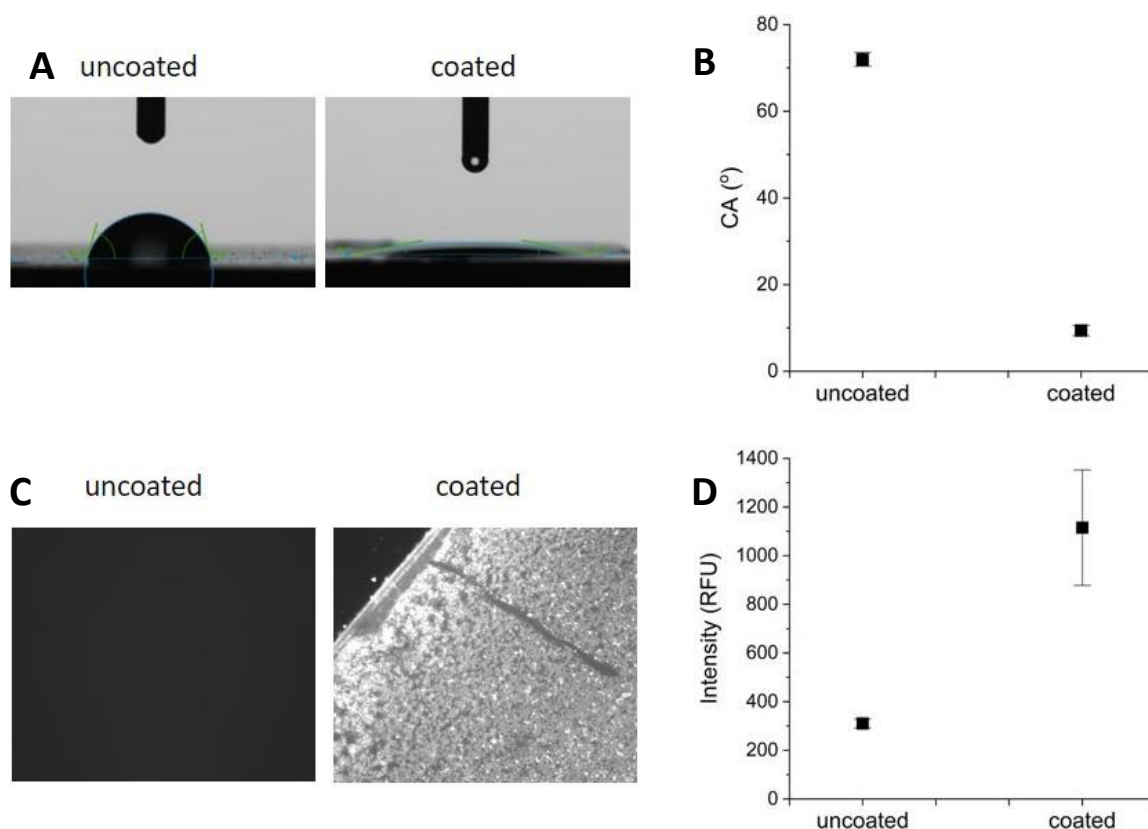


**Fig. S1.** Validation of Coating presence on UMR Material. (A) images of sessile drops of deionized water from contact angle measurements on uncoated and coated samples. (B) average contact angle values. (C) micrographs of UMR material without and with fluorescently-labelled coating. Images represent a 2173  $\mu\text{m}$  x 1818  $\mu\text{m}$  (3.95 mm<sup>2</sup>) area. (D) averaged fluorescence intensity of UMR material without and with fluorescently-labelled coating.

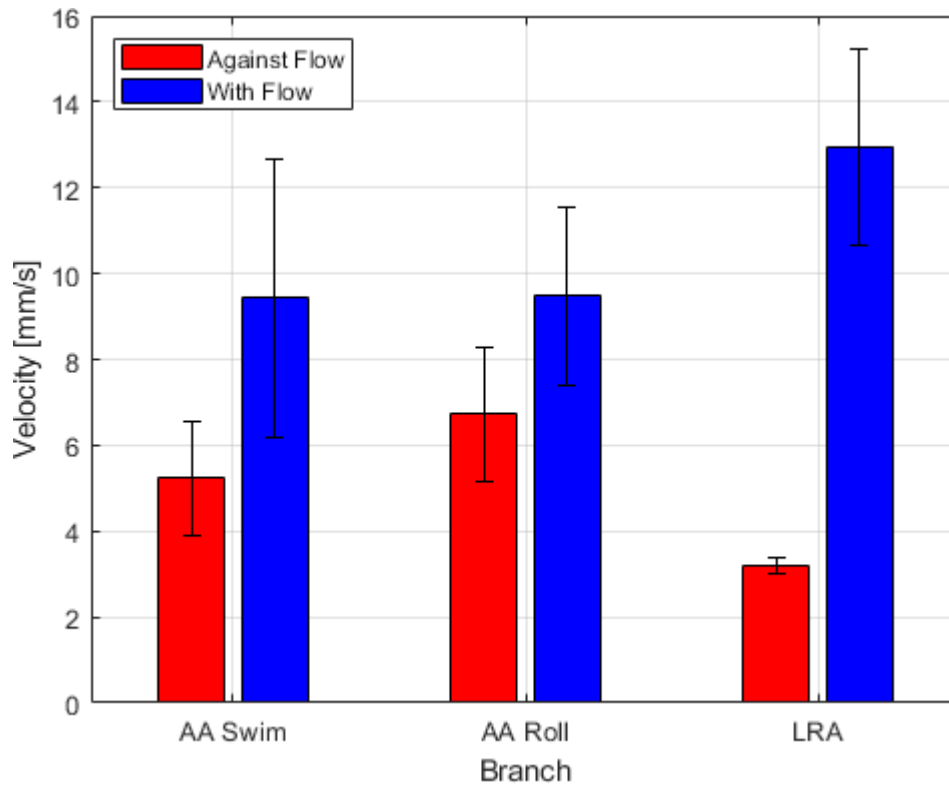


**Fig S2.** The velocities of the UMR against and with flow in during swimming and rolling and various arteries (Abdominal Aorta and Left Renal Artery) in *ex vivo* conditions.

Table S1. Artery dimensions of the *ex vivo* models

	Inner Diameter [mm]
Abdominal Aorta	9.8-14.7
Left Renal Artery	4.2-6
Right Renal Artery	4.6-6

Table S2. Design parameters of the UMRs

	12 mm long millirobot	9 mm long millirobot
Length Total [mm]	12.66	9.495
Diameter Total [mm]	5	3.75
Diameter inner cylinder [mm]	1.2-2.5	0.9-1.875
Fin thickness [mm]	0.5	0.375
Fin pitch [mm]	3.6-12	2.9-9

**Movie S1. Magnetic actuation of an UMR inside the Abdominal aorta and the left renal artery of the *ex vivo* perfusion model.** The trajectory shown of the UMR inside the abdominal aorta and renal artery corresponds to Figure 7A and 7C. The rotational frequency of the RPM was teleoperated using live acquisition of X-ray images. The X-ray acquisition frame rate is 5 frames per second. The videos are played back in real time and the trajectory of the UMR is overlayed on top of the video.

**Movie S2. UMR swimming trajectories exposed to a blood flow range from 15 to 67 ml/min an *ex vivo* abdominal aorta.** Both the 12-mm-long and 9-mm-long UMR are actuated at 9 Hz and exposed to various blood flow rates, corresponding to Figure 6. The X-ray acquisition frame rate is 5 frames per second. The videos are played back in real time and the trajectories of the UMRs are overlayed on top of the videos.

**Movie S3. UMR locomotion mechanism when exposed to a rotating magnetic field and an out-of-plane magnetic torque.** The 9-mm-long UMR is actuated at 9 Hz, while exposed to an out-of-plane torque of the RPM. The resulting angle of the UMR corresponds to the angle visualised in Figure S1 and illustrates the locomotion mechanisms used to enter the left renal artery, Figure 7C. The video was captured at 30 Hz and is played back in real time.

**Movie S4. *Ex vivo* Navigation of UMRs though the abdominal aorta and execution of a turning maneuver into the left renal artery.** Navigation of the UMR in *ex vivo* conditions corresponds to the image shown in Figure 8B and 8C. The navigation was done under two conditions, with and without blood flow in the abdominal aorta. The rotational frequency of the RPM was teleoperated using live acquisition of X-ray images. The X-ray acquisition frame rate is 2 frames per second. The videos are played back in real time and the trajectories of the UMR are overlayed on top of the videos.

## Supplementary Files

This is a list of supplementary files associated with this preprint. Click to download.

- [MovieS1.mp4](#)
- [MovieS2.mp4](#)
- [MovieS3.mp4](#)
- [MovieS4.mp4](#)